

# Combined Effects of Thermal Non-equilibrium and Chemical Reactions on Hypersonic Air Flows around an Orbital Reentry Vehicle

Jun Hyeok Chae<sup>1</sup>, Tapan K. Mankodi<sup>1</sup>, Seong Man Choi<sup>2</sup>, Rho Shin Myong<sup>1</sup>

<sup>1</sup>School of Mechanical and Aerospace Engineering & Specialized Graduate School of Aerospace Engineering & ReCAPT, Gyeongsang National University, Jinju 52828, Republic of Korea  
and

<sup>2</sup>Department of Aerospace Engineering, Chonbuk National University, Jeonju 54896, Republic of Korea

## Abstract

The present work computationally investigated the combined effects of thermal non-equilibrium and chemical reactions on hypersonic air flows around an orbital reentry vehicle during its reentry. The chemically reacting gas flow around the orbital vehicle was simulated for actual reentry trajectories, with a computational solver based on the Navier-Stokes-Fourier equations. Hypersonic flows for a wide range of flying altitudes from 40 km to 80 km were examined. We first analyzed important properties such as Mach number, trans-rotational temperature, vibrational temperature, chemical species composition, and surface properties such as the maximum heat flux for various altitudes. We then investigated the distribution of heat flux on the surface of the orbital reentry vehicle and the coupled effects of thermal non-equilibrium and chemical reactions on the hypersonic air flows. The computed heat flux results were compared with actual flight test data obtained during reentry of the orbital vehicle. The computed results were found to be in excellent agreement with the flight test data until an altitude of 60 km. Finally, we propose an explanation why heat flux was over-predicted around 70 km altitude but returned to better agreement at the higher altitude of 80 km. The phenomenon is based on two competing effects: the shortcoming of the first-order law of heat flux in the NSF equations and the inaccurate description of the effects of thermal non-equilibrium on chemical reactions in Park's two temperature model.

**Key words:** Hypersonics; reentry vehicle; CFD; heat flux; chemical reaction

## 1. Introduction

As interest in hypersonic flight and reentry has increased, several research groups around the world have been developing the critical technology needed for reentry flight safety and commercialization. Primarily because of its relatively low cost and few limitations, computational analysis has been increasingly adopted in recent decades to investigate and model reentry flow physics, and is now widely used to predict performance for the design of efficient hypersonic vehicles. Reentry vehicles pass through several layers of Earth's atmosphere, each with different ambient conditions, during their descent. The high Mach number flow around the reentry vehicle is dominated by high-temperature thermo-chemical physics associated with molecular dissociation and ionization. This high-temperature effect will influence the surface temperature and heat flux of the vehicle, which acts as a thermal load. The extent of the heat flux and heat load depends on the shape of the vehicle and its flight altitude. Accurate calculation of the heat load is therefore important when designing the flight trajectory, and the thermal protection system (TPS) that endures the heat on the nose frontal surface. Although computational research in this field has expanded in recent times, further research on the combined effects of thermal non-equilibrium and chemical reactions using the latest computational techniques are needed to fully comprehend the flow physics in hypersonic non-equilibrium flows around reentry vehicles.

Theoretical and experimental research on hypersonic reentry flight has been actively pursued since 1950. Several computational fluid dynamics (CFD) analyses, such as predicting the aerodynamic database of the Beagle 2 Mars-type atmospheric entry probe [1] and aerodynamic heating studies on the high-temperature effects of reentry flows, including the effects of reaction chemistry [2] have been undertaken. A study on the aerodynamic heating of the European intermediate experimental vehicle (IXV) at high altitudes and the effect of high temperature reacting gases during hypersonic reentry [3] has also been undertaken.

In addition, Lee and Park [4] investigated the effects of the nose radius of a blunt body on aerodynamic heating in a thermo-chemical non-equilibrium flow. Kim *et al.* [5] analyzed whether the continuum based computational methods were valid in rarefied air flows above 100 km and simulated

rarefied flows around a sub-orbital reentry vehicle using the Navier-Stokes-Fourier (NSF) code. Kang *et al.* [6] focused on the importance of high-temperature reacting gas effects on reentry vehicle flow fields. Min and Lee [7] conducted reentry analysis and risk analysis for end-of-life disposal of a multi-layer LEO satellite. Ivanovich *et al.* [8] investigated the aerodynamic characteristics of a spacecraft vehicle in the transitional regime using the local engineering method and three gas-surface interaction models.

Figure 1 shows the various trajectories of reentry vehicles through earth's atmosphere for different missions. In general, the reentry vehicles have similar trajectory patterns, although their initial reentry speeds are significantly different. For instance, the reentry speed during the Stardust reentry capsule's descent in the Earth's atmosphere was much higher than those encountered by other reentry vehicles, and it led to a high level of ionization in the flow field. In contrast to the Stardust reentry capsule, other reentry vehicles, such as the Japanese orbital reentry experiment (OREX) vehicle, descended at a lower speed and the flow around the vehicle was dominated by nitrogen dissociation. With further reduction in altitude and speed, hypersonic flows become dominated by oxygen dissociation and vibrational excitation. These processes are also highlighted in Fig. 1.

In this study, we conducted a detailed investigation of the combined effects of thermal non-equilibrium and chemical reaction on hypersonic air flows around an orbital reentry vehicle during descent. For this purpose, among various re-entry vehicles shown in Fig. 1, we selected the OREX vehicle, since it provided comprehensive information about atmospheric conditions and thermal data for a wide range of altitudes (48-105 km). The OREX vehicle was launched by the H-II rocket on Feb. 4, 1994, from the Tanegashima Space Center in Japan. Various types of flight data were obtained about the thermal environment the OREX vehicle experienced during its flight [10].

For the OREX vehicle, we focused on the effect of thermal non-equilibrium and chemical reaction on the shock front, and the maximum heat flux over its entire descent trajectory. The lowest altitude chosen for our computational simulations was 40 km. At this altitude the ambient conditions conform to the near local-thermal-equilibrium assumption, and it has been well established that the NSF-based CFD simulations are valid. The highest altitude chosen for our simulations was 80 km. In contrast to

flows at lower altitudes, the atmospheric conditions encountered at such high altitudes lead to high Knudsen numbers, and the flow belongs to the transition regime.

To simulate hypersonic flows at altitudes as high as 80 km, it would be interesting to examine the validity and limitations of the NSF code based on the first-order constitutive relations using the recent second-order constitutive relations developed from the Boltzmann kinetic equations. In particular, it would be worthwhile to investigate the combined effects of thermal non-equilibrium and chemical reactions on the predicted maximum heat flux at such high altitude, and the reason behind the deviation between the NSF predictions and the actual flight data. From these analyses, we will carefully explore the subtle interplay between the effects of thermal non-equilibrium and chemical reaction leading to this deviation.

In the following sections, we first describe the governing equations for mixed gases to take into account the effects of high temperature chemically reacting gas in hypersonic flows. We then describe the computational method based on the density-based finite volume solver and the physical input parameters and the ambient conditions at various altitudes the OREX vehicle experienced during its reentry. We also present details of the chemical reaction model and the TPS characteristics of the OREX vehicle. After a detailed CFD simulation, we analyze the flow properties such as Mach number, trans-rotational temperature, vibrational temperature, and chemical species composition; and surface properties such as wall heat flux distributions; and in particular, the maximum heat flux as a function of altitude. Finally, we compare the CFD results with the peak heat flux from the actual OREX flight test data.

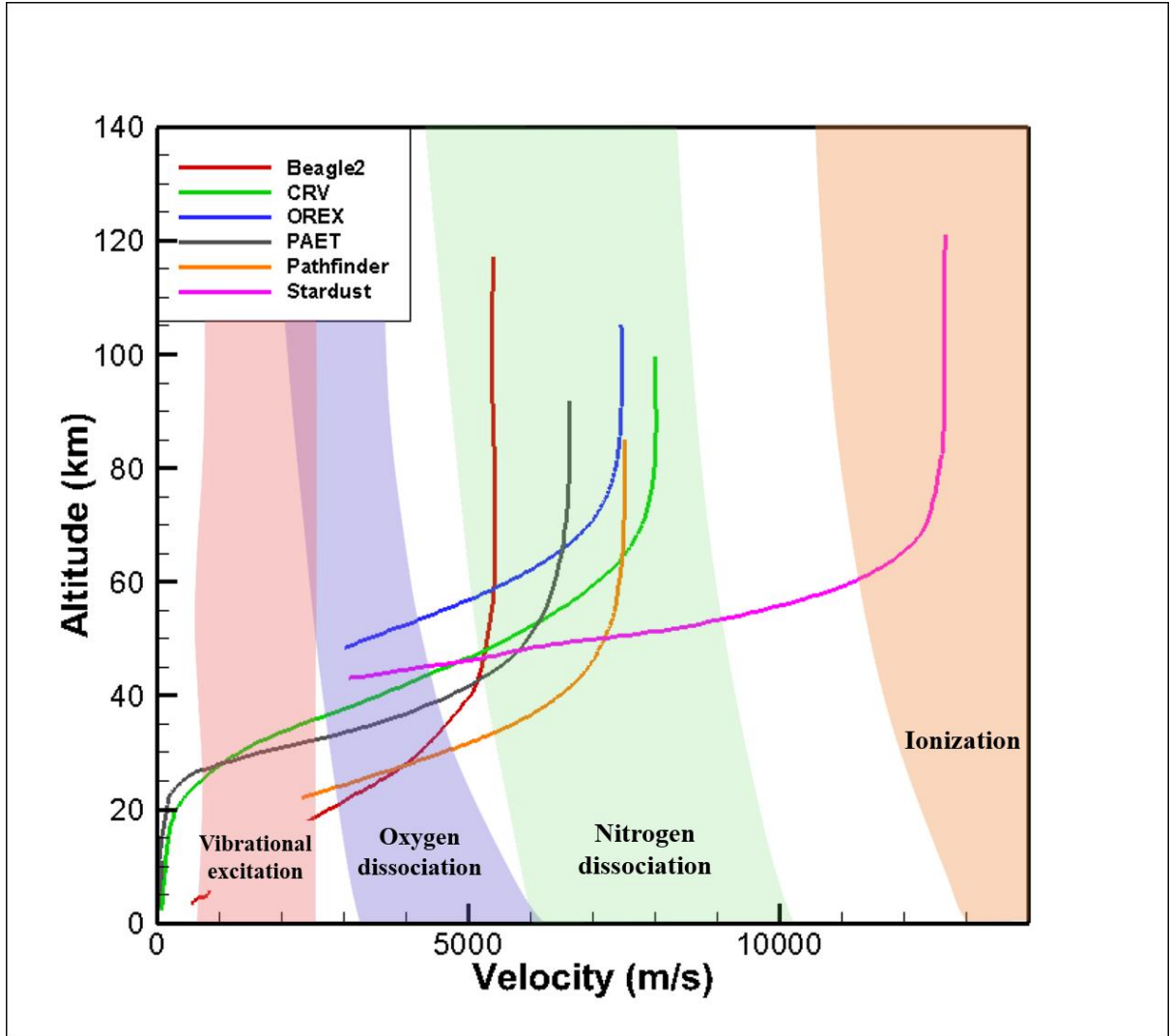


**Fig. 1 Trajectories of various reentry vehicles through Earth's atmosphere**

## 2. Governing Equations

In general, the macroscopic NSF equations based on the first-order constitutive laws are assumed to be valid up to an altitude of 60 km. At higher altitudes, mesoscale kinetic methods such as the direct simulation Monte Carlo (DSMC) should be used to account for the rarefaction effects of gas in the aerothermodynamic analysis. However, the DSMC is computationally very demanding, especially for the range of altitudes from 40 to 65 km. As a practical alternative, we employ the NSF equation as a first approximation at altitudes over 60 km, even though it may not be an ideal approach. It can be argued that this choice is not entirely inappropriate since the study is focused on how to properly handle the thermochemical non-equilibrium effects and provide engineering data efficiently for

designing the TPS of the reentry vehicle.

The NSF equations for a single gas can be extended to mixed gases to take into account the effects of high temperature chemically reacting gas in hypersonic flows [11]. The conservation of mass for a single gas is given as,

$$\frac{\partial \rho}{\partial t} + \frac{\partial}{\partial x_j} (\rho u_j) = 0 \quad (1)$$

where  $\rho$  is the mixture density and  $u_j$  is the mass averaged velocity in the  $j_{th}$  direction.

The conservation of momentum equations in the summation notation can be written as,

$$\frac{\partial}{\partial t} (\rho u_i) + \frac{\partial}{\partial x_j} (\rho u_i u_j) = \frac{\partial}{\partial x_j} [-(p + \frac{2}{3} \rho k) \delta_{ij} + \tau_{ij}] \quad (2)$$

where  $p$  is the pressure,  $k$  is the turbulent kinetic energy,  $\delta_{ij}$  is the Kronecker delta and  $\tau_{ij}$  is the shear stress tensor. For laminar viscous flows or algebraic turbulence models, the turbulent kinetic energy,  $k$ , is not present in the equation. This form of the momentum equations is valid for both calorically perfect and multi-species gases.

The conservation of total energy per volume is given as,

$$\frac{\partial E_t}{\partial t} + \frac{\partial}{\partial x_j} [(E_t + p) u_j] = \frac{\partial q_j}{\partial x_j} + \frac{\partial}{\partial x_i} (u_j \tau_{ij}) - \frac{\partial}{\partial x_j} (\sum_{s=1}^{ns} h_s J_{sj}) \quad (3)$$

where  $E_t$  is the total energy per volume,  $q_j$  is the heat flux in the  $j_{th}$  direction, and the last term in the right-hand side represents the effect of heat transfer due to species molecular diffusion.

The remaining governing equations are related to chemistry and multiple energy modes. These equations are called the thermo-chemical equations. The conservation of mass for each species or mixture fraction is given as,

$$\frac{\partial \rho_s}{\partial t} + \frac{\partial}{\partial x_j} (\rho_s u_j) = \frac{\partial J_{sj}}{\partial x_j} + \omega_s \quad (4)$$

where  $\rho_s$  is the species or mixture density,  $J_{sj}$  is the mass diffusivity flux in the  $j_{th}$  direction, and  $\omega_s$  is the source term associated with the reaction of species,  $s$ . The conservation of mass equation is replaced by the conservation of species mass equations if mixing or chemical reactions are included.

The mixture density is obtained as,

$$\rho = \sum \rho_s \quad (5)$$

Another remaining conservation equation for the molecular vibrational energy per volume is given as,

$$\frac{\partial E_v}{\partial t} + \frac{\partial}{\partial x_j} (E_v u_j) = \frac{\partial}{\partial x_j} \left( \sum_s e_{v,s} J_{s,j} - q_{v,j} \right) + \omega_v \quad (6)$$

where  $E_v$  is the molecular vibrational energy per volume,  $e_{v,s}$  is the molecular energy per mass for the species  $s$ ,  $q_{v,j}$  is the heat flux of vibrational energy in the  $j_{th}$  direction, and  $\omega_v$  is the source term associated with the potential difference between the vibrational energy and the equilibrium energy of the mixture.

The vibrational energy equation is based on the assumption that all molecular species can be represented by one vibrational temperature. A more general approach would treat each molecular species separately, which will result in a vibrational temperature and vibrational energy equation for each species. Finally, the vibrational energy equation represents either the conservation of vibrational energy or the conservation of the combined vibrational-electronic energy of the mole.

### 3. Simulation Methodology

#### 3.1 Computational method

In the present work, CFD-FASTRAN, a density-based compressible NSF code for chemically reacting multi-species gases was employed to simulate the hypersonic flow around the OREX vehicle. Temperature-dependent transport properties were used to handle the high-temperature gas effects. The implicit Roe's solver was used to calculate numerical fluxes to accurately capture the shock wave and the viscous boundary layer. A second-order reconstruction method and van Leer flux limiter were employed to maintain monotonicity in the shock region.

Along with the energy equation, an additional equation for the vibrational energies for the molecular constituents of the gas was considered. Further, the effect of thermal non-equilibrium on chemical reactions was handled by employing the widely used Park's two temperature model [12]. Because energy across the shock wave is very high, it is necessary to include the chemical reactions.

Finite rate chemistry was employed to handle the dissociation, exchange and recombination reactions pertaining to the air chemistry.

The Menter's SST  $k-\omega$  turbulence model for the Reynolds averaged Navier-Stokes (RANS) equations was employed to describe the turbulent boundary layer near the wall, which might be formed at relatively low altitudes. In the present simulations, the  $k-\epsilon$  turbulence model showed a good convergence in the overall flow region, but required an additional near-wall treatment for achieving enough accuracy near the wall. In contrast, the  $k-\omega$  turbulence model was shown to be highly accurate in the vicinity of the wall, but its high sensitivity to boundary conditions led to lower convergence rates in the free-flow region. On the other hand, the SST  $k-\omega$  model combines the advantages of the  $k-\epsilon$  and  $k-\omega$  models, and circumvents the shortcomings of the two models by employ the  $k-\omega$  model in the vicinity of the wall and the  $k-\epsilon$  model in the free-flow region.

### 3.2 OREX configuration and trajectory during descent

The details of the geometry and the boundary conditions for the OREX vehicle [13] are shown in Fig. 2. An important aspect of the geometry of the OREX vehicle is the aerodynamic deceleration device called the aeroshell. The aeroshell generates a large air resistance and protects the internal systems of the vehicle during reentry. The OREX nose cap, made of carbon/carbon (C/C) composite, is the heat and oxidation resistant material. The CFD-GEOM grid generation module was used to define the outer geometry of the OREX along with an appropriate domain. Necessary grid-independence studies were undertaken in order to obtain an optimized grid. It was found that results for the peak heat flux are consistent for simulations having total number of cells greater than 10,000. In the present simulations, a structured grid consisting of a total of 10,000 cells was used to simulate the hypersonic flow around the OREX geometry. The grid was sufficiently refined ( $y^+ < 1$ ) near the surface of the vehicle to accurately capture the laminar and turbulent boundary layers.

Four major boundary conditions were introduced at the initial problem set-up. Firstly, the far-field condition in the domain was employed to define the atmospheric ambient condition of altitude; the freestream gas speed, atmospheric temperature, and pressure. The details of the input conditions at



various altitudes are tabulated in Table 1 [10]. The turbulent kinetic energy ( $k$ ) and the specific rate of dissipation ( $\omega$ ) can be determined using the equations of  $k/U^2 = 10^{-6}$  and  $\omega c/U = 5$ , respectively [14]. Secondly, the radiative wall condition was imposed on the surface of the reentry vehicle. The radiative wall boundary condition handles the radiative heat flux at the wall according to the Stefan-Boltzmann law. The conditions for heat flux at the wall are a balance between heat conduction to the wall and radiation from it in the grid cell closest to the wall. The no-slip boundary condition was assumed at the wall as an approximation. Third, the extrapolated exit option was used at the outlet by extrapolating all flow variables from the interior of the domain. Thus the extrapolated option in this case requires no further information. Finally, the symmetry condition was assumed for the bottom face of the domain. By identifying the boundary as a symmetric boundary, the static pressure and the static temperature were extrapolated to the inner symmetric boundary, while the velocity was reflected along the symmetry plane.

Presently, the hypersonic flow was simulated with axisymmetric conditions to reduce the computational cost associated with three-dimensional simulations. However, the OREX vehicle may descend with a non-zero angle of attack, raising doubts about the validity of the axisymmetric flow assumption. Fortunately, it was shown from actual flight test data that the stagnation point remains very close to the center of the nose, justifying the axisymmetric flow assumption.

As stated in the previous paragraphs, the OREX flight data for velocity, temperature, and pressure were employed as the input conditions at the inflow boundary to simulate hypersonic flows at different altitudes.

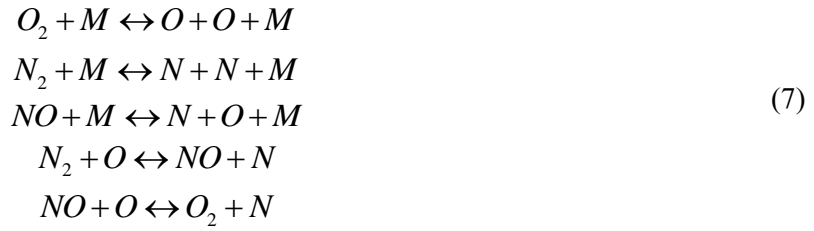
**Table 1. OREX flight test data [10]**

Flight Time (sec)	Altitude (km)	Velocity (m/s)	Temp. (K)	Press. (N/m <sup>2</sup> )	C/C Stag. Temp. (K)	Mach No.
7361.0	105.0	7451.0	217.5	0.0196	332	25.11
7370.6	101.1	7454.65	195.1	0.032	365	26.53
7381.0	96.77	7456.3	192.3	0.0726	422	26.71
7396.0	92.816	7454.1	188.7	0.163	492	26.97
7401.0	88.45	7444.3	186.87	0.231	587	27.07
7411.5	84.01	7415.9	188.9	0.594	690	26.82
7421.5	79.90	7360.2	198.64	1.0524	808	25.96
7431.5	75.81	7245.7	206.82	2.1717	928	25.04

7441.5	71.73	7049.2	214.98	4.023	1078	23.89
7451.5	67.66	6720.3	225.99	7.892	1251	22.22
7461.5	63.60	6223.4	237.14	14.02	1413	20.09
7471.5	59.60	5561.6	248.12	23.60	1519	17.55
7481.5	55.74	4759.1	258.74	39.48	1571	14.71
7491.5	51.99	3873.4	268.20	63.48	1557	11.8
7501.5	48.40	3000	270.62	98.50	1501	9.06

### 3.3 Chemical reaction model

In the present work, a five species air chemistry model consisting of atomic oxygen, atomic nitrogen, nitrous oxide, molecular oxygen, and molecular nitrogen was considered. A seventeen reaction model was also considered to account for the dissociation of molecules, exchange reactions known as the Zeldovich reactions, and recombination reactions. For example, the reactions in the five species gas model can be expressed as,



At high altitudes (>60 km), ionization reactions may also play an important role. However, neither the ionization reaction or ionized species and electrons were included in the analysis, since it is well accepted that the effect of ionization reactions is negligible when the stagnation point temperature is less than 9000K [15]. Seventeen reactions of dissociation, exchange and recombination were considered to account for the formation and disappearance of species. Two species (N<sub>2</sub>, O<sub>2</sub>) were estimated by applying elemental conservation relations, considering only the total density and conservation equations for the three chemical species (N, O, NO) [16]. The mass fraction of each species is shown in Table 2.

**Table 2. Mass fraction of species in the 5 species air chemistry model**

Species	N <sub>2</sub>	NO	N	O	O <sub>2</sub>
Mass fraction	0.747	0.001	0.001	0.001	0.25

The reaction rate coefficients were modeled using the Arrhenius equation. The two-temperature

model proposed by Park [12] was used to account for the thermal non-equilibrium in the flow. Table 3 shows the data of the pre-exponential factor ( $C_f$ ), the exponent of the temperature term ( $\eta_f$ ), and activation energy ( $E_a$ ) employed in the present chemical reaction analysis for calculating the chemical reaction rate constant coefficients ( $k_f$ ), respectively.

**Table 3. Constants employed in Arrhenius equation for calculating forward reaction rate coefficients [15]**

Reaction	M	$C_f$	$\eta_f$	$E_a$ (K)
<b>Dissociation reactions</b>				
$O_2 + M \leftrightarrow O + O + M$	O	$1.0 \times 10^{22}$	-1.5	59500
	N	$1.0 \times 10^{22}$	-1.5	59500
	NO	$2.0 \times 10^{21}$	-1.5	59500
	O2	$2.0 \times 10^{21}$	-1.5	59500
	N2	$2.0 \times 10^{21}$	-1.5	59500
$N_2 + M \leftrightarrow N + N + M$	O	$3.0 \times 10^{22}$	-1.6	113200
	N	$3.0 \times 10^{22}$	-1.6	113200
	NO	$7.0 \times 10^{21}$	-1.6	113200
	O2	$7.0 \times 10^{21}$	-1.6	113200
	N2	$7.0 \times 10^{21}$	-1.6	113200
$NO + M \leftrightarrow N + O + M$	O	$1.1 \times 10^{17}$	0.0	75500
	N	$1.1 \times 10^{17}$	0.0	75500
	NO	$1.1 \times 10^{17}$	0.0	75500
	O2	$5.0 \times 10^{15}$	0.0	75500
	N2	$5.0 \times 10^{15}$	0.0	75500
<b>Neutral/Zeldovich exchange reactions</b>				
$N_2 + O \leftrightarrow NO + N$		$1.8 \times 10^{14}$	0.0	38400
$NO + O \leftrightarrow O_2 + N$		$2.4 \times 10^9$	1.0	19220

### 3.4 Thermal protection system

The forebody of the OREX vehicle around the stagnation point is covered with the C/C nose cap thermal protection system. The C/C nose cap can withstand temperatures up to 2300K, which are far higher than the ceramic tile nose cap, which can accommodate about 1700K [17]. The C/C nose cap has a thickness of 4 mm and the material has a density of 1.5 g/cm<sup>3</sup>.

The surface emissivity of the thermal protection system (TPS) was applied to accurately calculate heat flux near the wall considering the surface radiation energy. The material re-radiates some of the heat back to the flow, and the amount depends on the emissivity of the material. It is also possible that the TPS material degrades through ablation (i.e., melting, vaporization, pyrolysis, etc.). In the present simulations, values of 0.84 and 0.7 were assumed for surface emissivity and for internal radiation, respectively.

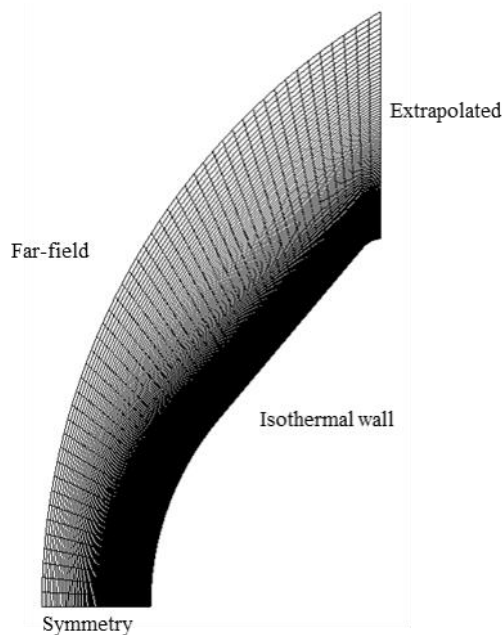


**Fig. 2 Grids and boundary conditions around the OREX vehicle**

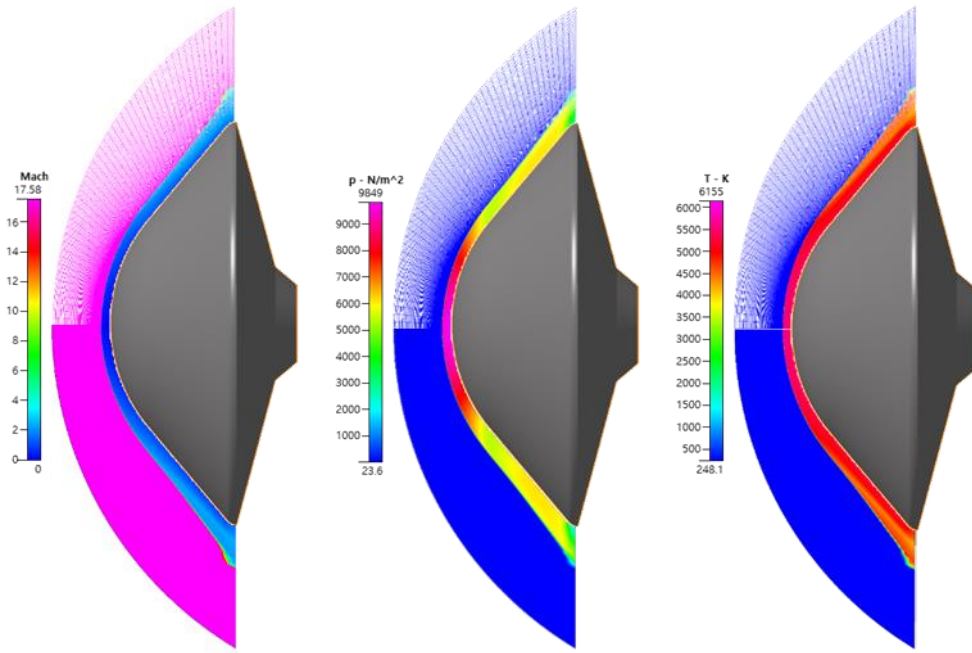


**Fig. 3 CFD calculations of chemically reacting flows around the OREX vehicle at 63.6km (Mach, pressure, temperature)**

#### 4. Results

In the present study, hypersonic air flows over the OREX vehicle were analyzed to understand the effects of thermal non-equilibrium and chemical reaction on the shock and the post-shock region. In particular, variations in the flow properties such as Mach number, temperatures and mole fractions of the constituents of the air, and surface properties such as the heat flux and coefficient of heat flux along the reentry surface as a function of trajectory and different altitudes, were examined in detail.

The contour plots of Mach number, pressure and trans-rotational temperature in the domain for ambient conditions at 60 km altitude are shown in Fig. 3. It is obvious that a strong bow shock is formed in front of the nose of the OREX vehicle. A quantitative comparative analysis of the flow properties along the stagnation line elucidated finer details of the flow chemistry and the non-equilibrium nature of the hypersonic flows.

##### 4.1 Flow properties along the stagnation line

###### 4.1.1 Mach number analysis

Figure 4 shows the variation in Mach number along the center line to the nose of the OREX reentry vehicle at different altitudes. It is evident that the shock standoff distance is smaller at a higher

altitude than at the lower altitude. The shock standoff distance at 48.48km is about 0.13m from the surface, but 0.08m at 59.60km, and 0.07m at 79.90km. This is a direct consequence of the fact that the smaller Mach number results in a shock front formed farther away from the surface of the vehicle. The shock standoff distance is proportional to the ratio of the free stream density to the post-shock density and the post-shock Mach number [18].

#### 4.1.2 Analysis of trans-rotational and vibrational temperatures

The high kinetic energy in the flow interacts with the surface of the vehicle and the kinetic energy transforms to thermal energy, forming a strong bow-shaped shock wave in the fore body of the vehicle. Figure 5 shows line plots of the trans-rotational temperature along the centerline from the freestream to the stagnation point at different altitudes. It is obvious that after the gas crosses the shock wave, the kinetic energy of the gas molecules transforms into thermal energy, causing the abrupt temperature rise and generating a high-temperature post-shock region. At an altitude of 79.90 km, it was observed that the maximum temperature in the flow field reaches 9300K. However, the shock standoff distance is the shortest, primarily due to high freestream Mach number. On the other hand, at the lowest altitude in our simulations, the maximum temperature is the lowest, but the shock is formed at the furthest distance from the surface of the vehicle.

The molecules in the pre-shock region have almost all their energy in kinetic modes. In the shock region, the molecules collide intensively among themselves and their kinetic energy is redistributed into thermal and internal energy. During this process, the translational and rotational relaxation time is much shorter than the vibrational relaxation time, since the number of collisions required to reach equilibrium in the former modes of energy is far less than that required for the latter case. Park's two temperature model [12] is based on this observation and assumes that the rotational and translational modes of energy equilibrate quickly, leading to a single value of trans-rotational temperature representing two modes of energies. On the other hand, the vibrational energy is represented by another property called the vibrational temperature.

The variation in the vibrational temperature along the stagnation line is shown in Fig. 6. With increasing altitude, the peak vibrational temperature increases. This is the case until 67.66 km altitude.

Beyond this altitude, it can be seen that the peak vibrational temperature decreases with a further increase in altitude.

A comparison of the peak trans-rotational and vibrational temperatures observed in the shock front at various altitudes is shown in Fig. 7. The difference between peak trans-rotational temperature and vibrational temperature clearly demonstrates the need for the thermal non-equilibrium model. That is, the degree of non-equilibrium can be easily identified by the significant difference in the peak trans-rotational temperature and the vibrational temperature, which are highlighted, and in particular, above the altitude of 65 km. With increasing altitude, the density of the ambient atmosphere rapidly decreases. As a result, the composite parameter measured by the product of the Knudsen number and Mach number increases significantly, leading to high level of thermal non-equilibrium.

#### 4.1.3 Effect of chemical reactions on the mole fractions

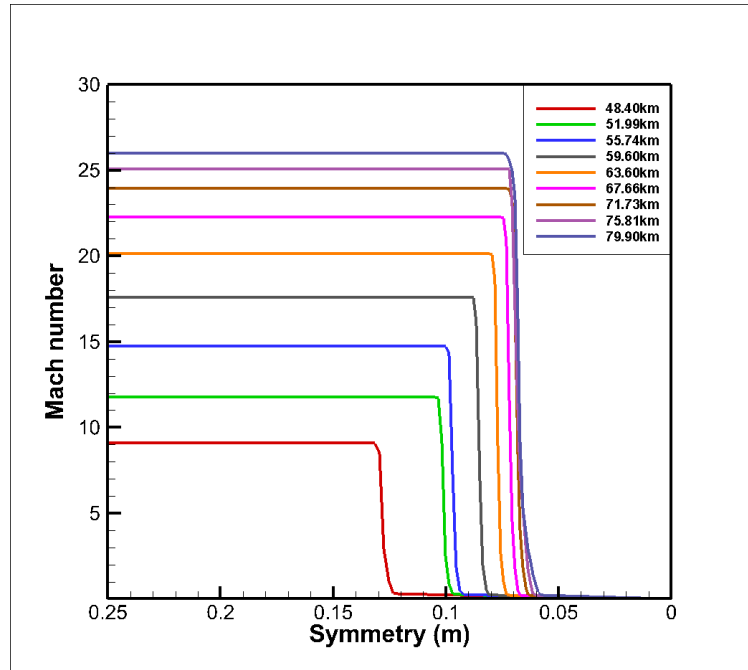
We examined the composition of gas and the distribution of five species in the shock and post-shock region. Figure 8 shows the mole fraction of nitrogen along the stagnation line at various altitudes. Molecular nitrogen has a mass fraction of 0.747 at ambient conditions in the pre-shock region. The molecule begins to dissociate in the post-shock region. As mentioned before, the nitrogen molecule starts to dissociate at around 4000K. It is apparent that with increasing temperature, the degree of dissociation of nitrogen increases. At 79.90 km, the temperature in the post-shock region was highest among the cases considered in this work. Nonetheless, it can be seen that nitrogen does not dissociate completely. Although the temperature was as high as 9300 K, it was not sufficient to dissociate all the molecules. This is primarily due to the high degree of thermal non-equilibrium, yielding an insufficient number of collisions for full dissociation.

Figure 9 shows the mole fraction of atomic nitrogen along the stagnation line at various altitudes. At the relatively low altitudes of 48.40 km and 51.99 km, the mole fraction of atomic nitrogen is negligible compared to those at higher altitudes, since the nitrogen molecules in the post-shock region with low temperature hardly dissociate. However, at altitudes higher than 55.74 km, a higher mole fraction of atomic nitrogen is observed in the post-shock region with high temperature. For example, at the altitude of 79.90 km, the contribution of atomic nitrogen approaches 0.5 in the mole fraction. In

addition to the dissociated nitrogen atoms recombining to produce molecular nitrogen, atomic nitrogen interacts with oxygen molecules to generate NO.

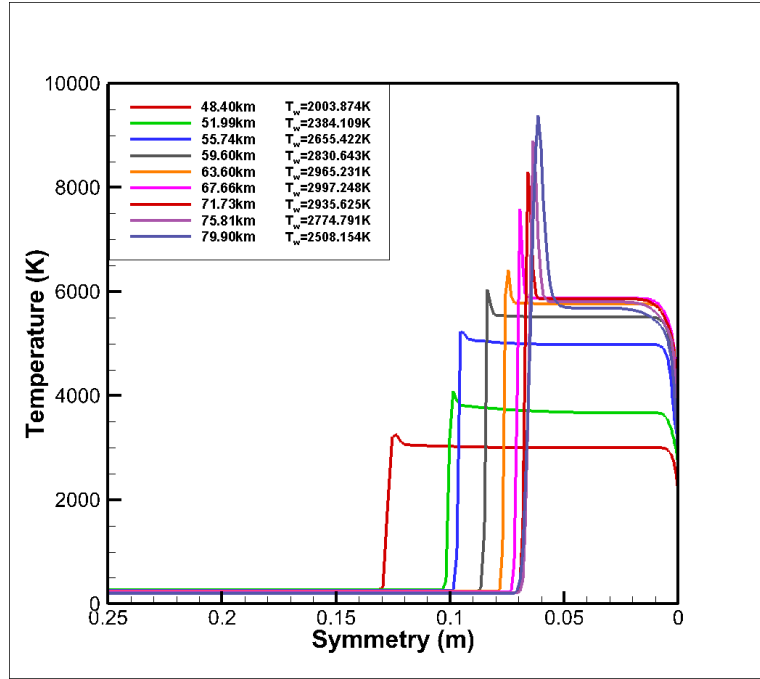
Figure 10 shows the mole fraction of molecular oxygen along the stagnation line at various altitudes. It is apparent that the degree of dissociation is higher than molecular nitrogen shown in Fig. 8. Compared with nitrogen molecules, oxygen molecules have a much lower dissociation temperature. Therefore, even at relatively low altitudes of 48.40 km and 51.99 km, the degree of dissociation of molecular oxygen is substantial, since the post-shock temperatures are high enough for molecular oxygen to dissociate. For higher peak temperatures at higher altitudes, molecular oxygen completely dissociates in the post-shock region.

Figure 11 shows the mole fraction of atomic oxygen along the stagnation line at various altitudes. The number of oxygen atoms rapidly increase in the shock region as more oxygen molecules dissociate across the shock wave. With increasing altitudes, the mole fraction of atomic oxygen gradually increases and reaches an asymptotic value of 0.25 at altitudes above 55.74 km. On the other hand, at lower altitudes, it was observed that oxygen atoms can combine with molecular nitrogen and produce a small amount of NO.



**Fig. 4 Variation in Mach number along the stagnation line at different altitudes**





**Fig. 5** Variation in the trans-rotational temperature along the stagnation point and temperature at the wall ( $x=0$ ) at different altitudes

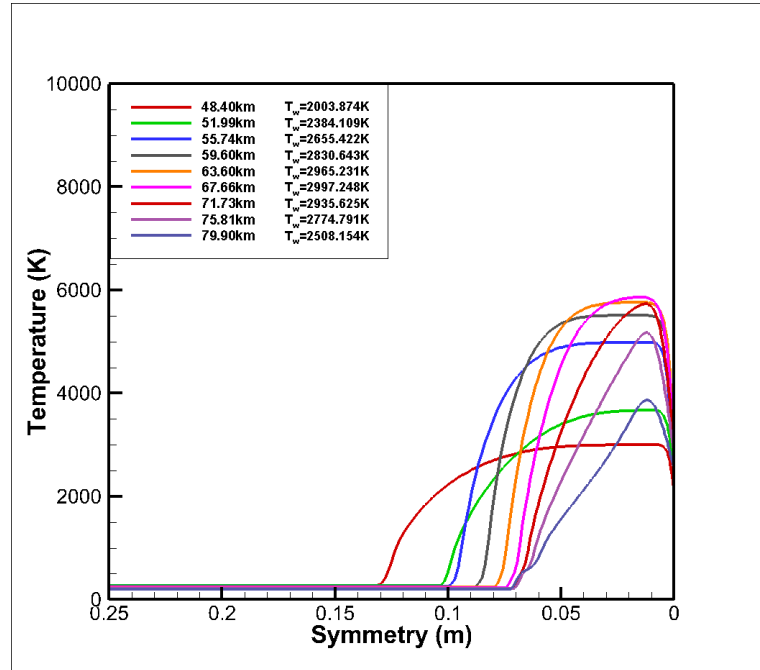


**Fig. 6** Variation in the vibrational temperature along the stagnation point and temperature at the wall ( $x=0$ ) at different altitudes

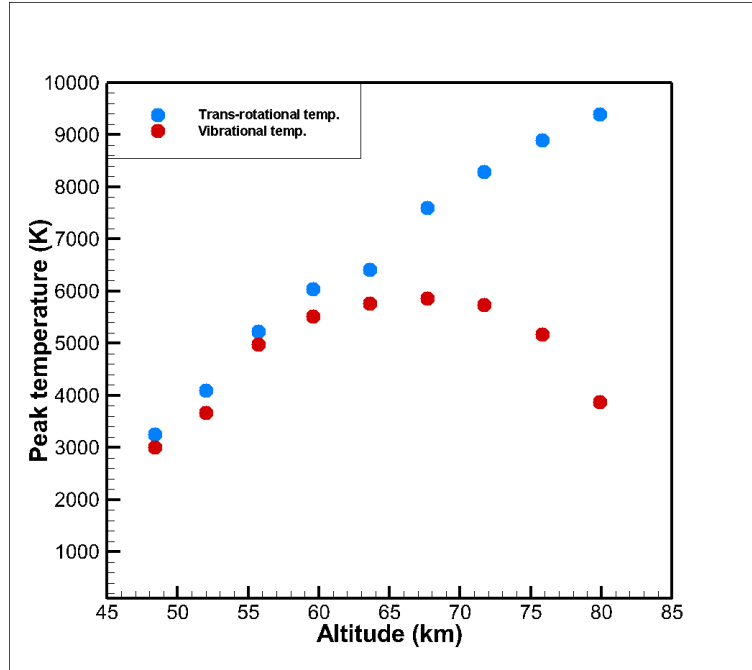


**Fig. 7 Peak trans-rotational and vibrational temperatures in the shock front at various altitudes**

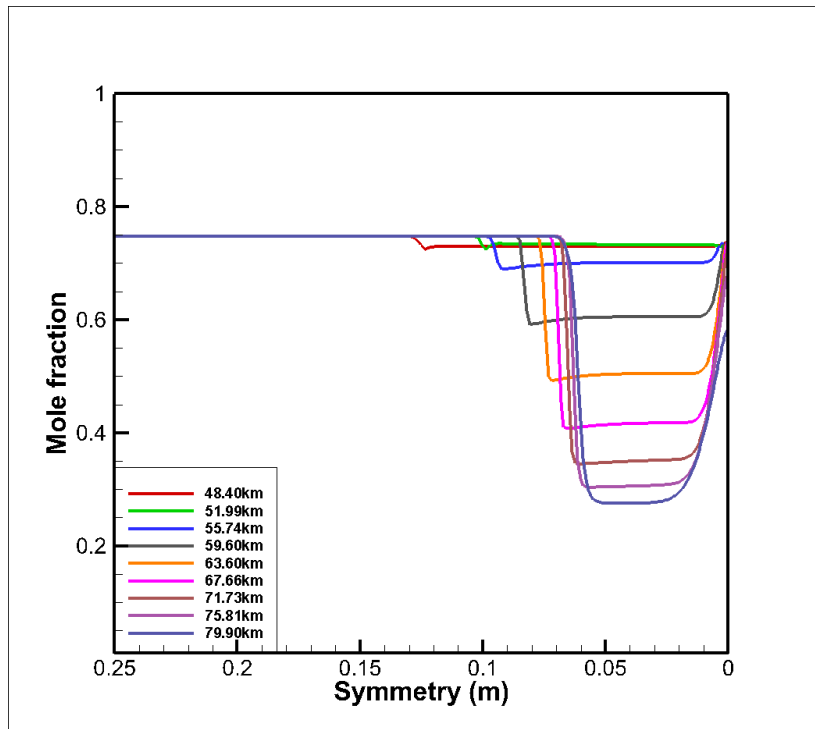


**Fig. 8 Variation in the mole fraction of  $N_2$  along the stagnation line at different altitudes**

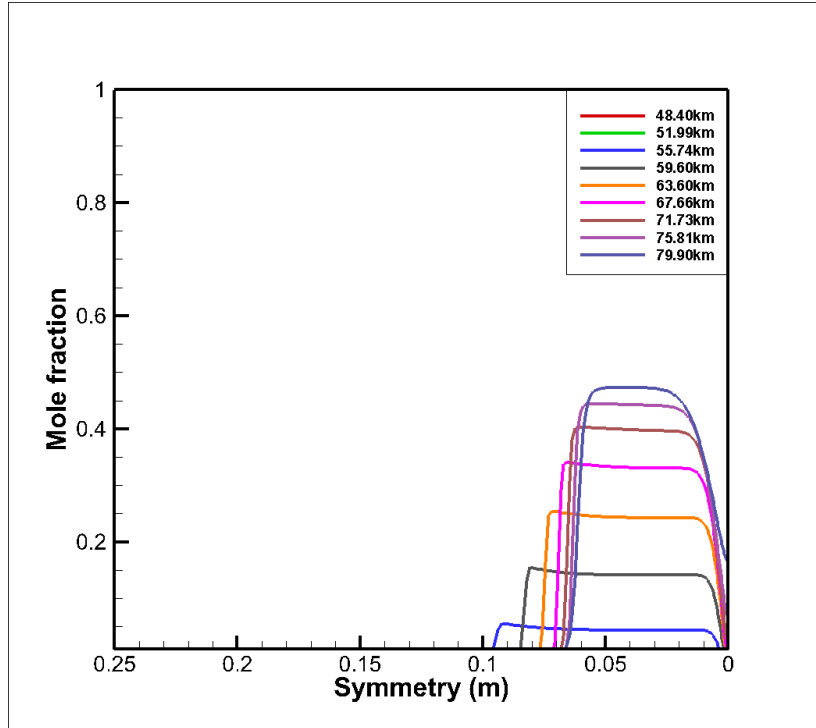


**Fig. 9 Variation in the mole fraction of N along the stagnation line at different altitudes**

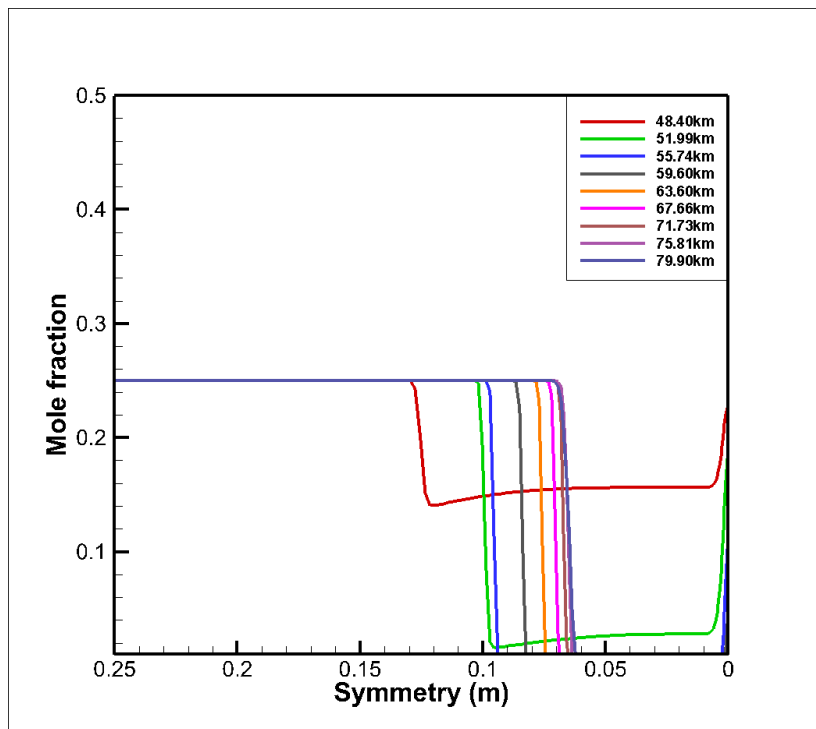


**Fig. 10 Variation in the mole fraction of  $O_2$  along the stagnation line at different altitudes**

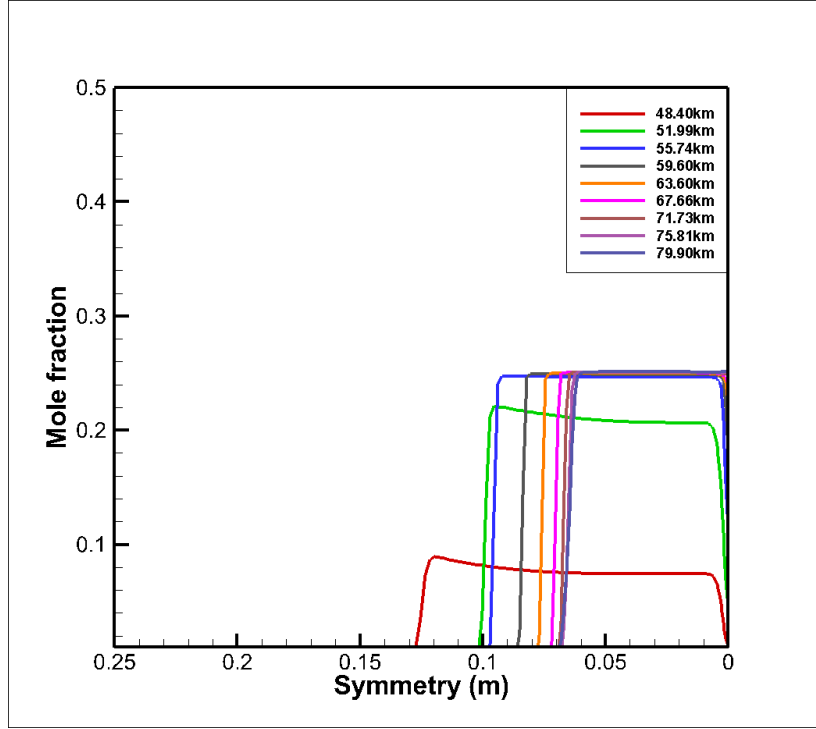


**Fig. 11 Variation in the mole fraction of O along the stagnation line at different altitudes**

Figure 12 shows the distribution of the mole fraction of molecular nitrogen and the trans-rotational temperature (or the geometric mean of the trans-rotational and vibrational temperatures  $\sqrt{T_{tr}T_{vib}}$  in Park's two temperature model [12]) at the highest altitude of 79.90 km and the lowest altitude of 48.40 km considered in the present study. At the highest altitude, a significant portion of molecular nitrogen was found to dissociate in the post-shock region near the nose of the OREX vehicle. In contrast, at the lowest altitude, it was observed that the degree of dissociation of molecular nitrogen was much lower even in the shock front, since the temperature was too low for intense dissociation of molecular nitrogen. This difference between the highest and lowest altitudes can be explained by Fig. 12 (c) which illustrates the distribution of the trans-rotational temperature relative to the threshold temperatures needed to dissociate molecular nitrogen and oxygen, 4000K and 2500K, respectively.

Figure 13 shows the distribution of the mole fraction of molecular oxygen at the highest and lowest altitudes. At the highest altitude, it shows complete dissociation of molecular oxygen in the post shock region. In particular, the complete dissociation of molecular oxygen occurs not only near the central

stagnation region but also uniformly at all frontal sections of the vehicle. This feature can again be explained by Fig. 12 (c) and the distribution of the trans-rotational temperature, which clearly shows that the temperature in all the post-shock regions is higher than the threshold temperature needed for the dissociation of molecular oxygen, 2500K. Like the molecular nitrogen, the degree of dissociation of molecular oxygen gradually decreased with increasing altitudes. It is noteworthy that the degree of dissociation of molecular oxygen is higher than that for molecular nitrogen even at lower altitudes. This is because oxygen molecules dissociate around 2500K, which is much lower than the threshold temperature for the dissociation of nitrogen, 4000K.

Finally, the mole fraction of NO along the stagnation line at various altitudes is shown in Fig. 14. Unlike other chemical species, NO has a different distribution pattern. Once the flow encounters the shock wave, the mole fraction of NO abruptly increases because the dissociated oxygen and nitrogen molecules or dissociated nitrogen and molecular oxygen immediately recombine to produce NO. It can also be seen that with increasing altitudes, the mole fraction of NO increases until the critical altitude of 51.99 km. Beyond this altitude, the mole fraction of NO starts to decrease. The increasing pattern is due to the combination of oxygen atoms and nitrogen molecules, which is prominent at the altitude of 48.40 km. From the altitude of 48.40 km to the critical altitude of 51.99 km, the increasing pattern is due to the increase in atomic nitrogen in the flow, leading to enhanced interactions with molecular oxygen and more NO through exchange reactions. On the other hand, the reason for the decreasing pattern beyond the critical altitude of 51.99 km is because NO can easily dissociate into oxygen and nitrogen atoms.

#### 4.2 Effect of thermal non-equilibrium

The variation in the peak trans-rotational and vibrational temperatures in the shock front at various altitudes is shown in Fig. 7. It should be noted that the ratio of vibrational temperature to trans-rotational temperature decreases with increasing altitudes, highlighting the increasing importance of the degree of non-equilibrium with increasing altitudes. In addition to this ratio, the degree of non-equilibrium can be calculated using a novel parameter introduced by Myong [19-21]. The non-equilibrium parameter can be defined as follows,

$$N_\delta \equiv \frac{\tau}{p} = \frac{\mu V / L}{p} = \sqrt{\frac{2\gamma}{\pi}} Kn \cdot M = \gamma \frac{M^2}{Re} \quad (8)$$

where  $\mu$  is the Chapman-Enskog viscosity,  $V$  is the velocity,  $L$  is the characteristic length, and  $\gamma$  is the ratio of specific heats.

As explained in detail by Myong [19], the degree of thermal non-equilibrium in *phase space* is best represented by the Knudsen number, since the collision integral of the Boltzmann kinetic equation in dimensionless form is scaled by the inverse Knudsen number. However, when the non-equilibrium effects are described in the *macroscopic thermodynamic space*, it is straightforward to identify two—in contrast with just one in the case of the *microscopic phase space*—primary dimensionless parameters  $Re$  and  $M$ . This is accomplished by comparing inertial force  $\rho u^2$ , hydrostatic pressure  $p$ , and viscous force  $\tau$  in the conservation of law of momentum; the former being the ratio of inertial force to viscous force, and the latter the ratio of inertial force to hydrostatic pressure.

In a similar fashion, a composite parameter can be defined as the ratio of viscous force  $\tau$  to the hydrostatic pressure  $p$  and this can best represent the degree of thermal non-equilibrium in *macroscopic thermodynamic space* because the viscous force is a direct consequence of the thermal non-equilibrium effect. In gas flows near the local-thermal-equilibrium, pressure dominates over viscous stress. In other words, the diagonal elements of the stress tensor dominate over the off-diagonal terms. However, this is not true in the case of high non-equilibrium flow conditions. That is, the off-diagonal terms of the stress tensor are no longer negligible compared to the diagonal term  $p$ .

Figure 15 shows the variation in the maximum non-equilibrium parameter in the shock front with increasing altitudes. It is apparent that at altitudes below 60 km, this parameter is far smaller than unity, suggesting a near-equilibrium condition. However, beyond 60 km, the parameter is of the order of unity, indicating a high degree of thermal non-equilibrium.

Using the first-order constitutive relations based on Navier's law of viscous stress and Fourier's law of heat flux can be justified when the non-equilibrium parameter is small. At a high degree of non-equilibrium, however, it is in principle necessary to include the second-order effects on the viscous stress and heat flux. Figure 16 compares the heat flux predicted by the first-order Fourier's law and

the second-order nonlinear coupled constitutive relation (NCCR) [19-21]. It highlights the non-negligible role of second-order effects at a high degree of non-equilibrium; in particular, the over-prediction of heat flux by the first-order NSF equations.

### 4.3 Surface properties

#### 4.3.1 Heat flux along the re-entry surface

The heat flux in any direction, say the  $j_{th}$  direction,  $q_j$ , can be calculated using Fourier's law of heat conduction [22]. This relationship can be written as,

$$q_j = -(\kappa + \kappa_t) \frac{\partial T}{\partial x_j} \quad (9)$$

where  $\kappa$  is the thermal conductivity of the gas,  $\kappa_t$  is the turbulent thermal conductivity,  $T$  is the gas temperature. The thermal conductivity and the turbulent thermal conductivity are related to the laminar and turbulent viscosity coefficients as follows:

$$\kappa = \frac{\mu C_p}{Pr}, \quad \kappa_t = \frac{\mu_t C_p}{Pr_t} \quad (10)$$

where  $Pr$  and  $Pr_t$  are the Prandtl number and turbulent Prandtl number, respectively, and  $C_p$  is the heat capacity.

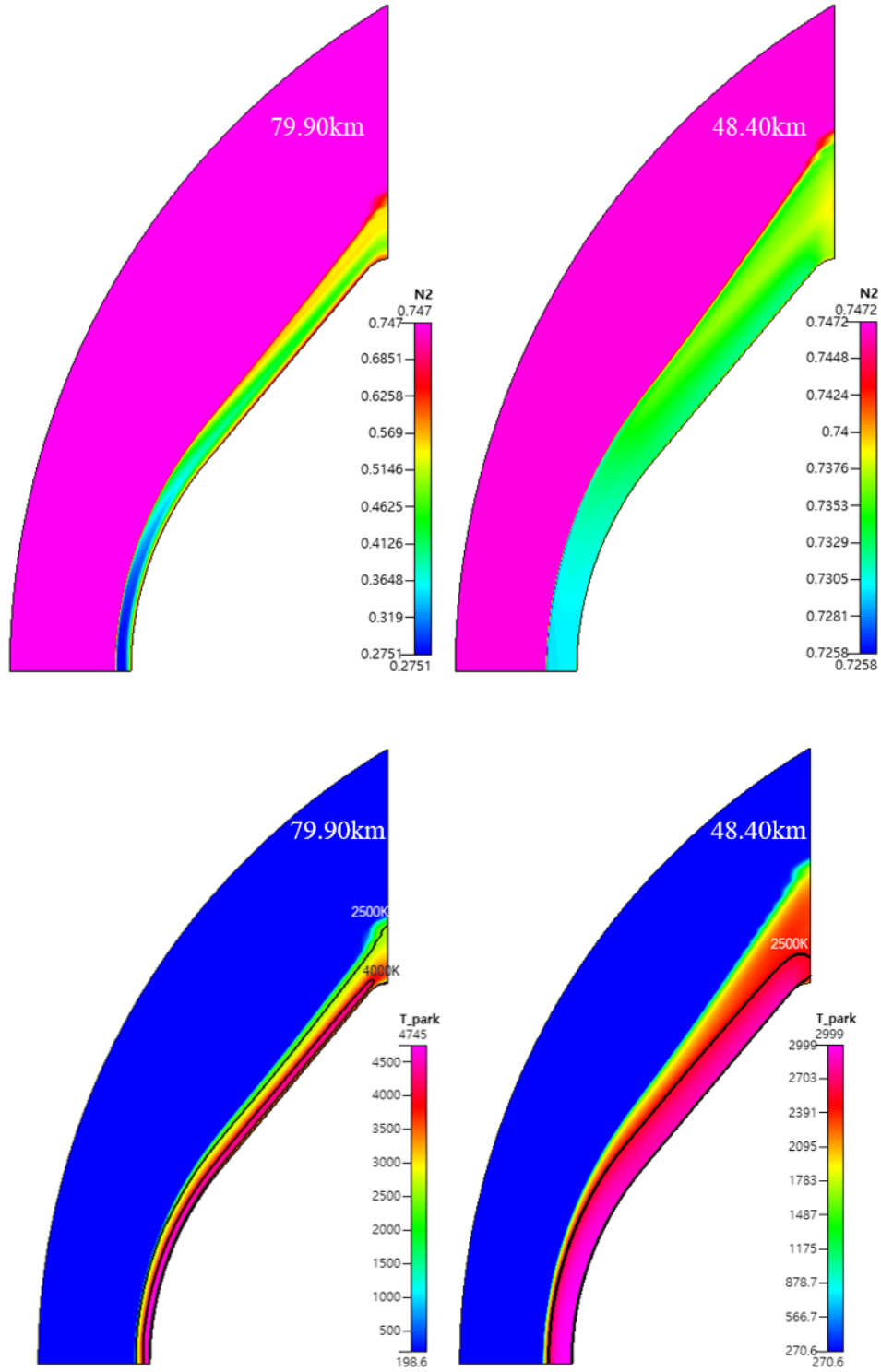


**Fig. 12** Contour plots of molecular nitrogen and Park's temperature  $\sqrt{T_w T_{vib}}$  ; a) mole fraction at 79.90 km, b) mole fraction 48.40 km, c) Park's temperature at 79.90km, d) Park's temperature at 48.40km



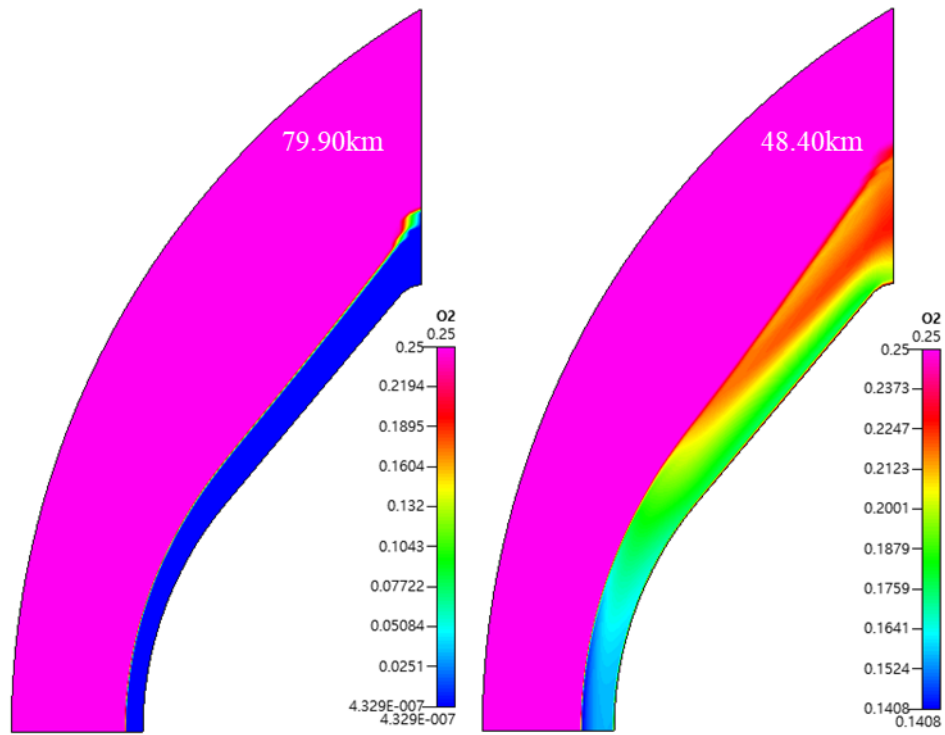


Fig. 13 Contour plots of molecular oxygen at a) 79.90 km and b) 48.40 km

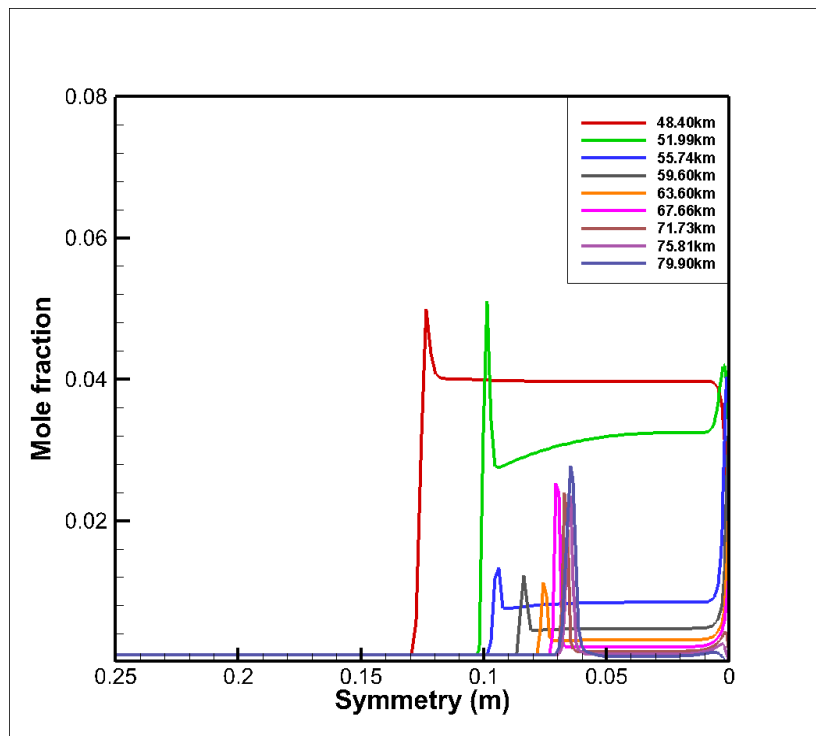
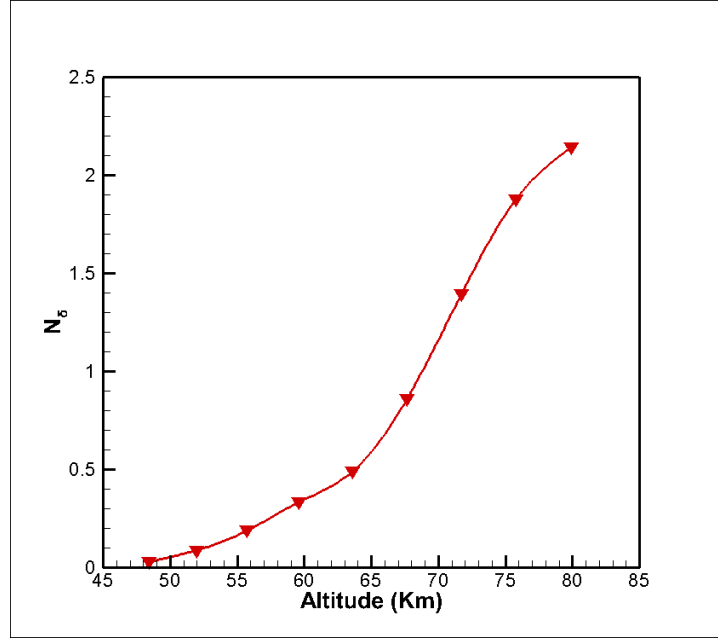
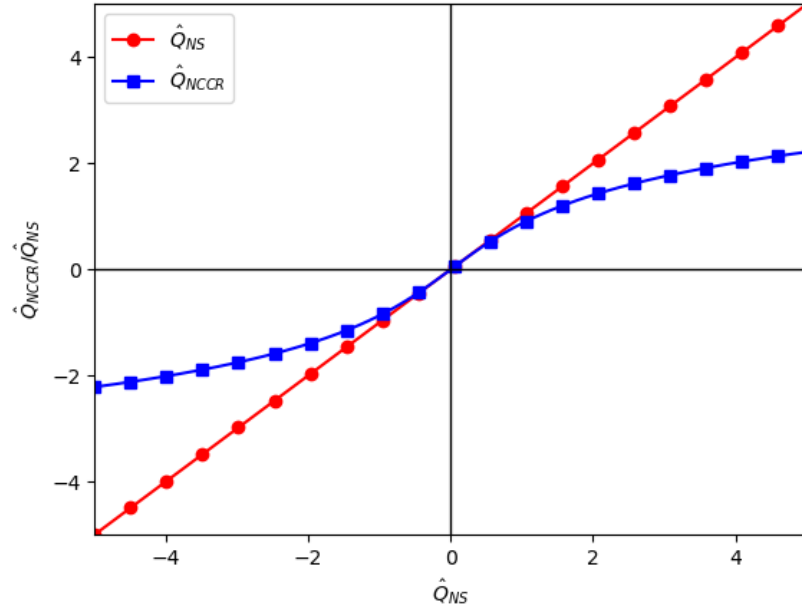


Fig. 14 Variation in NO along the stagnation line at different altitudes



**Fig. 15** The peak value of thermal non-equilibrium parameter  $N_\delta$  at different altitudes



**Fig. 16** Comparison of heat flux  $\hat{Q}$  between the first-order NS and the second-order NCCR

For thermal non-equilibrium flows, Fourier's laws for trans-rotational and vibrational energy are given by

$$q_j = -(\kappa_{tr} + \kappa_t) \frac{\partial T}{\partial x_j} \quad (11)$$

$$q_{v,j} = -\kappa_v \frac{\partial T_v}{\partial x_j} \quad (12)$$

where  $\kappa_{tr}$  is the translational-rotational thermal conductivity and  $q_{v,j}$  is the vibrational heat flux in the  $j_{th}$  direction,  $\kappa_v$  is the vibrational thermal conductivity, and  $T_v$  is the vibrational temperature of the gas.

Figure 17 shows the distribution of heat flux on the surface of the OREX vehicle at three different altitudes: a) 63.6 km, b) 67.66 km (the altitude where maximum heat flux is observed) and c) 71.73 km. For each altitude, it shows that the peak heat flux value is observed at the nose of the vehicle, which is also the stagnation point. The heat flux subsequently decreases in a radial direction to the wall surface. Interestingly, an additional local peak is observed in the elbow region of the frontal surface of the OREX vehicle [23]. This phenomenon occurs because the decrease in temperature near the corner produced by local expansion enhances recombination, and as a result, the additional heat of formation is injected into the region, ultimately producing a local peak in the wall heat flux.

#### 4.3.2 Peak heat flux

The high Mach number flow around the OREX vehicle is dominated by high-temperature thermochemical mechanisms like molecular dissociation and ionization. This high-temperature effect can significantly affect the heat flux of the vehicle and the extent of the heat flux. An accurate calculation of the heat flux remains essential when designing the thermal protection system (TPS) that protects the internal system from harsh thermal environments.

Figure 18 compares the CFD results with the actual OREX flight test data [24]. It can be seen that the heat flux rapidly increases with increasing altitude, reaches a maximum, and then decreases with increasing altitude. The maximum heat flux is observed between 65 km and 70 km. This is closely related to differences in ambient density, and the speed of the reentry vehicle. The reentry vehicle decelerates using atmospheric friction as it descends into the denser, lower part of Earth's atmosphere. In this process, the competing effects of decreasing freestream velocity and increasing ambient density result in a maximum heating at a certain altitude.

In the present simulation, the center of the nose of the OREX vehicle was assumed to be a stagnation point, since it was shown from actual flight test data that the stagnation point remains very close to the center of the nose.

Additional simulations were carried out with the same inputs but with fully catalytic boundary condition on the vehicle surface. The results of peak heat fluxes obtained with fully catalytic boundary conditions are added to Fig. 18 for comparison. It is apparent that heat fluxes calculated with fully-catalytic boundary condition are greater than those calculated with non-catalytic boundary condition. And the heat flux data obtained with the non-catalytic boundary condition is closer to the experimental data. Thus, it is reasonable to judge that the catalytic effects are not that strong in the present case. A similar observation was reported in the study of Gupta *et al.* [25] on orbital reentry experiment (OREX).

Upon comparing the experimental and numerical results with non-catalytic wall boundary condition, it is apparent that at lower altitudes, the match between the two is excellent. However, there is a significant difference between the two data at altitudes higher than 60 km. It is suggested that the difference in this case is due to shortcomings of the physical model employed in our study; that is, the linear NSF model based on not-far-from-equilibrium and no-slip boundary condition. It was noted in Fig. 15 that the non-equilibrium parameter—the product of the Knudsen and Mach numbers—increases with increasing altitudes. It was also shown in Fig. 16 that at higher degrees of non-equilibrium, the heat flux predicted by the NSF equations is greater than the actual heat flux. These two critical findings explain why the present NSF code over-predicts the maximum heat flux at altitudes higher than 60 km (with  $N_\delta \approx 0.33$ ) when compared to the actual flight test data.

Interestingly, at the highest altitude of 80 km, the experimental data and the numerical results obtained with non-catalytic wall boundary condition again agree excellently with each other. This counter-intuitive result may be due to the interplay of two major thermodynamic effects: the non-equilibrium effect on non-conserved quantities (heat flux in this case) and the non-equilibrium effect on chemical reactions. The reason behind this result can be understood from a molecular point of view.

At a molecular level, with increasing rarefaction, the number of collisions decreases, while the degree of non-equilibrium increases. A fraction of the collisions lead to dissociation-related chemical reactions where the collisional energy is greater than the bond enthalpy, leading to bond breaking. In

the case of rarefied flow with a high degree of non-equilibrium, calculating this fraction of collisions leading to dissociation is more complex than estimating such processes near thermal equilibrium conditions. It is well known that Park's two temperature model is a phenomenological model and has obvious limitations when estimating reaction rate coefficients in flows with a high degree of non-equilibrium, as demonstrated in a recent work by Mankodi and Myong [26]. Thus, the present NSF code based on Park's two temperature model will predict higher reaction rates and dissociation, which in turn leads to lower heat flux at altitudes above 60 km.

In summary, there are two competing effects which lead to the over-prediction of heat flux around 70 km altitude, but better agreement returns at higher altitudes. First, the shortcoming of the first-order law of heat flux in the NSF equations leads to a higher heat flux than the actual one. Second, the inaccurate description of the effects of thermal non-equilibrium on chemical reactions in Park's two temperature model leads to lower heat flux than the actual one. Around the altitude of 70 km, the incorrect usage of the first-order law dominates over the inaccurate non-equilibrium chemical reaction model, resulting in the peak heating greater than the actual one. On the other hand, at the highest altitude of 80 km, the two effects cancel each other out, leading to an excellent match with the actual flight test data.

In spite of the severe limitations of the pseudo-equilibrium based chemical reaction model, such as Park's two temperature model and the shortcoming of the first-order laws neglecting the second-order effects, it is noteworthy that the degree of deviation in the peak heat flux at altitudes higher than 60 km is not drastically troublesome. From the present study, it can be concluded that the accuracy of the NSF equations decreases with increasing altitudes, but for most engineering purposes, the estimation of heat flux based on the NSF laws and Park's two temperature model is within reasonable bounds, at least, for the hypersonic flows experienced by the OREX vehicle. In addition to the peak heat flux results, the other properties such as surface pressure distribution were also compared with computational results reported by Gupta *et al.* [25] and were found to be in excellent agreement.

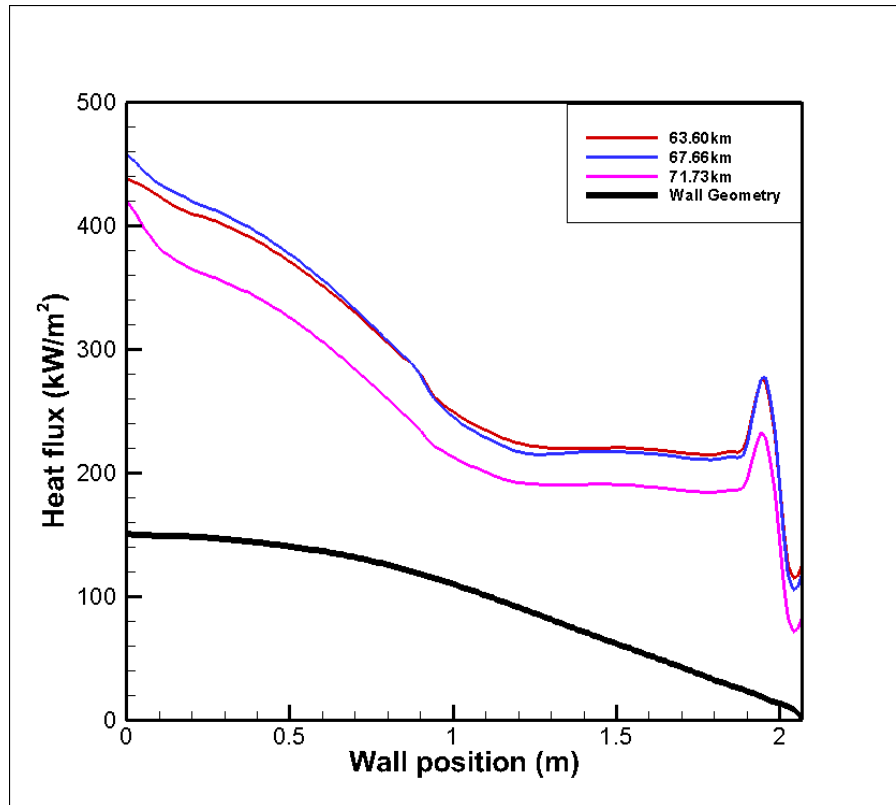


Fig. 17 Wall heat flux distribution on the frontal surface of the OREX vehicle

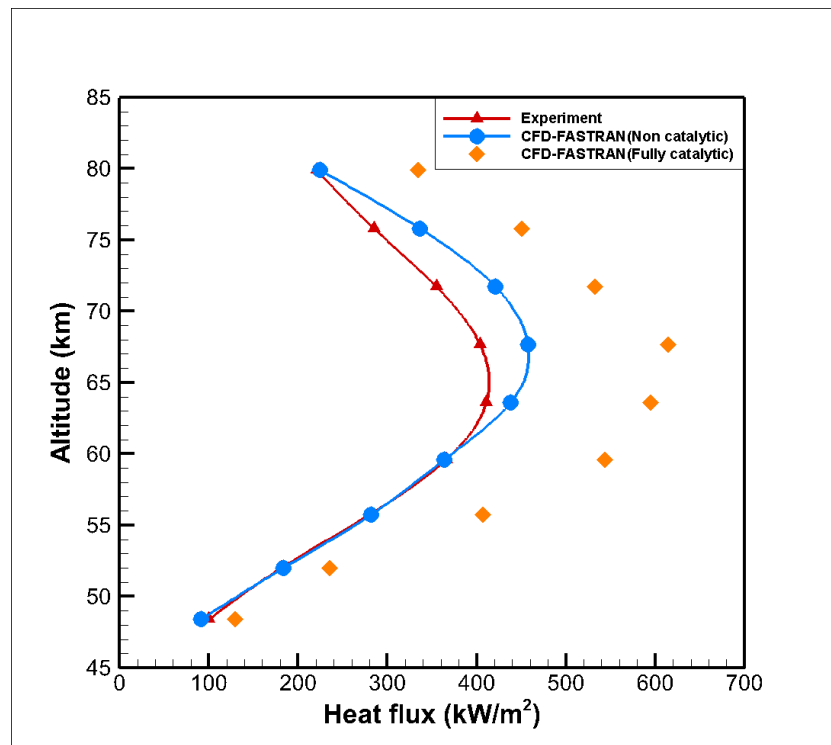


Fig. 18 Comparison of the CFD results with the OREX flight test data for the maximum heat flux at different altitudes

## 5. Conclusion

We investigated the effect of thermal non-equilibrium and chemical reactions on the shock front and maximum heat flux over the entire descent trajectory of the OREX vehicle. We also analyzed important properties such as Mach number, trans-rotational temperature, vibrational temperature, chemical species composition, and surface properties such as the maximum heat flux as a function of altitude.

The trans-rotational temperature was predicted to reach maximum at the highest altitude of 79.90 km, because this corresponds to the highest re-entry speeds. On the other hand, the vibrational temperature was predicted to reach maximum at the altitude of 67.66 km. The difference between the maximum trans-rotational temperature and vibrational temperature clearly demonstrates the need for a proper model of thermal non-equilibrium.

The degree of dissociation of molecular nitrogen was found to increase with increasing temperature similar to the dissociation of molecular oxygen. However, a faster and higher degree of dissociation of oxygen molecule was observed in the same temperature zones, since the bond enthalpy of the oxygen molecule is much lower than that of the nitrogen molecule. In particular, molecular oxygen completely dissociated not only near the central stagnation region but also uniformly at all frontal sections of the vehicle at altitudes higher than 55.74 km.

An accurate calculation of heat flux remains essential when designing a proper thermal protection system, which protects the reentry vehicle from harsh thermal environments. In this context, the CFD results for the maximum heat flux were carefully compared with the actual OREX flight test data. The maximum heat flux was observed between 65-70 km altitudes for both CFD and flight test data. This is closely related to the fact that the reentry vehicle decelerates using atmospheric friction as it descends into the denser, lower part of Earth's atmosphere, and the competing effects of decreasing freestream velocity and increasing ambient density result in a maximum heating at a certain altitude.

In addition, the match between CFD and flight test data was shown to be excellent at lower altitudes. However, the deviation between the two data became significant at altitudes higher than 60 km. The gap in this case is argued to be due to shortcomings of the NSF model based on not-far-from-

equilibrium. Since the heat flux predicted by Fourier's law is greater than the actual heat flux at a higher degree of non-equilibrium, the present NSF code over-predicts the maximum heat flux at altitudes higher than 60 km.

Further, the puzzle of why heat flux was over-predicted at around 70 km altitude but was in better agreement at the higher altitude of 80 km was explained to result from two competing effects: the shortcoming of the first-order law of heat flux in the NSF equations, and the inaccurate description of the effects of thermal non-equilibrium on chemical reactions in Park's two temperature model. The former effect—the over-prediction of heating load by the first-order Fourier law—dominates around the altitude of 70 km, while the former and latter effects cancel out at the highest altitude of 80 km, leading to an excellent match with the actual flight test data.

At the same time, the present study provides additional motivation towards developing the second-order law of heat flux and more accurate models of the effect of thermal non-equilibrium on chemical reactions. We hope to report the investigation of these subjects in near future.

### **Acknowledgement**

This work was supported by the National Research Foundation of Korea (NRF) Grant funded by Ministry of Science and ICT (NRF-2017M1A3A3A03016312).

### **References**

1. Liever PA, Habchi SD, Burnell SI, Lingard JS (2003) Computational fluid dynamics prediction of the Beagle 2 aerodynamic database. *Journal of Spacecraft and Rockets* 40(5):632-638
2. Lee M (1998) Aerodynamic heating prediction of reacting blunt body flow with an impinging shock wave. *International Heat Transfer Conference Digital Library*, Begel House Inc.
3. Roncioni P, Ranuzzi G, Marini M, Paris S, Cosson E, Walloschek T (2011) Experimental and numerical investigation of aerothermal characteristics of hypersonic intermediate experimental vehicle. *Journal of Spacecraft and Rockets* 48(2):291-302
4. Lee CH, Park SO (2003) Effects of nose radius of blunt body on aerodynamic heating in thermochemical nonequilibrium Flow. *Journal of Computational Fluids Engineering* 8(4):34-40



5. Kim C, Lee Y, Lee D (2008) Aerodynamic analysis of sub-orbital re-entry vehicle. *Journal of Computational Fluids Engineering* 13(2):1-7
6. Kang E, Kim J, Park J, Myong RS (2014) Computational investigation of the high temperature reacting gas effects on re-entry vehicle flowfields. *Journal of Computational Fluids Engineering* 19(1):7-14
7. Min C, Lee D (2018) Reentry analysis and risk assessment for end-of-life disposal of a multi-layer LEO satellite. *International Journal of Aeronautical and Space Sciences* 19(2):496-508
8. Ivanovich KY, Myint ZYM, Yurievich KA (2013) Aerodynamics investigation for prospective aerospace vehicle in the transitional regime. *International Journal of Aeronautical and Space Sciences* 14(3):215-221
9. Khlopkov YI, Chernyshev SL, Myint ZYM, Khlopkov AY (2016) Effects of gas-surface interaction models on spacecraft aerodynamics. *International Journal of Aeronautical and Space Sciences* 17(1):1-7
10. Yamamoto Y, Yoshioka M (1995) CFD and FEM coupling analysis of OREX Aerothermodynamic Flight Data. 30th Thermophysics Conference
11. CFD-FASTRAN User Manual, ESI CFD Inc, 2017
12. Park C (1990) Nonequilibrium Hypersonic Aerothermodynamics. Wiley, New York
13. Yoshinaga T, Tate A, Watanabe M, Shimoda T (1996) Orbital re-entry experiment vehicle ground and flight dynamic test results comparison. *Journal of Spacecraft and Rockets* 33(5):635-642
14. Spalart PR, Rumsey CL (2007) Effective inflow conditions for turbulence models in aerodynamic calculations. *AIAA Journal* 45(10):2544-2553
15. Hansen F (1958) Approximations for the thermodynamic and transport properties of high-temperature air. NACA Technical Note 4150
16. Kim S, Lee HJ (2018) Quasi 1D nonequilibrium analysis and validation for hypersonic nozzle design of shock tunnel. *Journal of the Korean Society for Aeronautical & Space Sciences* 46(8):652-661

17. Yamamoto M, Atsumi M, Yamashita M, Imazu I, Morita S (1996) Development of C/C composites for OREX (orbital reentry experimental vehicle) nose cap. *Advanced Composite Materials* 5(3):241-247
18. Sinclair J, Cui X (2017) A theoretical approximation of the shock standoff distance for supersonic flows around a circular cylinder. *Physics of Fluids* 29(2):026102
19. Myong RS (1999) Thermodynamically consistent hydrodynamic computational models for high-Knudsen-number gas flows. *Physics of Fluids* 11(9):2788-2802
20. Myong RS (2004) Gaseous slip model based on the Langmuir adsorption isotherm. *Physics of Fluids* 16(1):104-117
21. Myong RS (2016) Theoretical description of the gaseous Knudsen layer in Couette Flow based on the second-order constitutive and slip-jump models. *Physics of Fluids* 28(1):012002
22. White F (1991) *Viscous Fluid Flow*. 2nd edition McGraw-Hill, New York
23. Takahashi Y, Yamada K (2018) Aerodynamic heating of inflatable aeroshell in orbital reentry. *Acta Astronautica* 152:437-448
24. Doihara R, Nishida M (2002) Thermochemical nonequilibrium viscous shock layer studies of the orbital reentry experiment (OREX) vehicle. *Shock Waves* 11(5):331-339
25. Gupta RN, Moss JN, Price JM (1996) Assessment of thermochemical non-equilibrium and slip effects for orbital reentry experiment (OREX). 31st AIAA Thermophysics Conference:1859
26. Mankodi TK, Myong RS (2019) Quasi-classical trajectory-based non-equilibrium chemical reaction models for hypersonic air flows. *Physics of Fluids* 31(10):106102